

High-performance broadband photodetectors based on b-As_{0.5}P_{0.5} for infrared optical communication and imaging

Qianli Ma (马千里)¹, Yiheng Li (李奕衡)¹, Dawei He (何大伟)², Yongsheng Wang (王永生)², and Yajie Yang (杨亚杰)^{2*}

¹School of Electronic and Information Engineering, Beijing Jiaotong University, Beijing 100044, China

²Key Laboratory of Luminescence and Optical Information, Ministry of Education, Institute of Optoelectronic Technology, Beijing Jiaotong University, Beijing 100044, China

*Corresponding author: yangyj@bjtu.edu.cn

Received November 14, 2024 | Accepted December 31, 2024 | Posted Online May 19, 2025

Infrared (IR) photodetectors (PDs) are crucial for medical imaging, optical communication, security surveillance, remote sensing, and gas identification. In this Letter, we systematically investigated a room temperature IR PD based on two-dimensional b-As_{0.5}P_{0.5}, a relatively unexplored component of b-AsP alloys. We synthesized high-quality b-As_{0.5}P_{0.5} flakes via the chemical vapor transport (CVT) method with precisely controlled conditions. The fabricated b-As_{0.5}P_{0.5} PD exhibits excellent photoconductivity, high responsivity, and a fast response in the visible and near-infrared (Vis-NIR) band. It achieves a responsivity of $\sim 0.209 \text{ A}\cdot\text{W}^{-1}$ and a response time of $\sim 16.6 \mu\text{s}$ under 1550 nm IR illumination. High-resolution single-pixel point optical imaging and high-speed optical communication were realized by the b-As_{0.5}P_{0.5} PDs. This study confirms that b-As_{0.5}P_{0.5} materials are highly promising for advanced IR optoelectronic applications.

Keywords: black arsenic-phosphorus; uncooled infrared photodetector; photoconductive effect; optical communication; infrared imaging.

DOI: [10.3788/COL202523.062501](https://doi.org/10.3788/COL202523.062501)

1. Introduction

Infrared PDs show a series of unique advantages in applications such as IR imaging, target identification, and temperature detection^[1-3]. Infrared PDs can be classified into two types: photon (typically cooled) and thermal (typically uncooled) PDs^[4]. Photon PDs work by generating electron-hole (*e-h*) pairs in the detector material when exposed to infrared (IR) radiation. They are the most sensitive and fastest form of IR detection, but they must operate at cryogenic temperatures to reduce thermally induced *e-h* pairs, which necessitates the use of cooling systems, adding to the system's size and cost. On the other hand, thermal PDs convert IR light by sensing a temperature-dependent physical property. These PDs do not require cooling, making them smaller and more power-efficient, but they are less sensitive and slower in response compared to photon PDs. However, with the emergence of 2D materials, uncooled photon PDs have been greatly developed. 2D materials have attracted significant attention due to their unique atomic hierarchical structure. Graphene (Gr) is the first extensively studied 2D material. Gr consists of a single layer of carbon atoms, characterized by very high carrier mobility and excellent electrical conductivity, along with strong light absorption across a wide range of wavelengths^[5-7]. Due to these outstanding properties, Gr is

considered an ideal candidate for the next generation of PDs. However, Gr has its limitations. While its excellent conductivity makes it highly suitable for electrical applications, Gr lacks an intrinsic bandgap, which restricts its effectiveness in certain optoelectronic applications, particularly in detectors requiring a high bandgap. Additionally, the fabrication cost of Gr is high, and the manufacturing process is complex, further limiting its large-scale commercial application^[8].

In addition to Gr, another 2D material that has garnered significant attention is black phosphorus (BP). BP is composed of phosphorus atoms, whose bandgap can be tuned from narrow (0.3 eV) to wide (2 eV) by adjusting its number of layers^[9,10]. BP exhibits very high carrier mobility, which demonstrates its significant potential in photodetection and electronic devices^[11]. However, BP is unstable in air and prone to oxidative degradation, resulting in a rapid decline in performance^[12], which significantly limits its practical applications. To address the instability of BP, researchers have conducted numerous modification studies, with the fabrication of black arsenic-phosphorus (b-AsP) through arsenic doping being a significant breakthrough^[13-16]. b-AsP retains the superior properties of BP, including its adjustable bandgap (0.15 to 0.3 eV) and high mobility while significantly enhancing environmental stability and extending its service life^[17]. b-AsP alloys with

varying arsenic-phosphorus ratios exhibit enhanced optoelectronic properties, making them strong candidates for PD applications^[18–24]. For instance, the hBN/b-As_{0.83}P_{0.17}/hBN sandwich-structure PD, developed by Yuan *et al.*, uses hexagonal boron nitride (hBN) and exhibits broad photoresponsivity (90 mA · W⁻¹) in the middle infrared (MIR) range and remarkable long-term air stability^[25]. The advent of b-AsP has opened new avenues for the development of novel uncooled IR detectors, particularly for PDs requiring long-term stable operation.

However, the b-AsP alloys with the b-As_{0.5}P_{0.5} component have not been deeply studied. Thus, this Letter seeks to investigate the b-As_{0.5}P_{0.5} component systematically. First, b-As_{0.5}P_{0.5} material was synthesized using the chemical vapor transport (CVT) technique. During the CVT process, reaction conditions, such as precursor gases, temperature, pressure, and gas flow, were precisely controlled to obtain high-quality and homogeneous b-As_{0.5}P_{0.5}. At room temperature, PDs based on b-As_{0.5}P_{0.5} demonstrate a broad spectral photoresponse from 520 to 1650 nm, with high responsivity (1.182–0.199 A · W⁻¹), high external quantum efficiency (282.1%–15.0%), and high detectivity (1.47 × 10⁸–2.48 × 10⁷ Jones). By employing a confocal optical system, the photoconductive effect (PCE) was confirmed as the photoresponse mechanism of b-As_{0.5}P_{0.5} PDs. Moreover, the b-As_{0.5}P_{0.5} PD exhibited fast response time of ~16.6 μs under 1550 nm IR illumination, showing high-speed real-time IR optical communication and high-resolution and high-sensitivity imaging capabilities. Our work, specifically focuses on the b-As_{0.5}P_{0.5} component, contributes to the study of b-AsP, and it offers deeper insights into its applications in communications and imaging. This study demonstrates that b-As_{0.5}P_{0.5} is a promising material for broad-spectrum IR photodetection, capable of meeting future high-performance requirements for IR optoelectronic applications.

2. Results and Discussion

The synthesized b-As_{0.5}P_{0.5} material is shown in Fig. 1(a). Arsenic and phosphorus atoms are alternately distributed in the b-As_{0.5}P_{0.5} single-atom layer, forming identical valence bonds in a 1:1 ratio. The larger radius of the arsenic atoms compared to the phosphorus atoms leads to an orthorhombic lattice with a wrinkled cellular structure. Each b-As_{0.5}P_{0.5} layer is held together by weak van der Waals (vdW) interactions, forming a bulk crystal. However, the weak interlayer forces make the b-As_{0.5}P_{0.5} crystals highly susceptible to exfoliation into monolayers. To verify the composition and crystal quality, the Raman spectra of the b-As_{0.5}P_{0.5} were analyzed, as shown in Fig. 1(b). Raman modes for b-As_{0.5}P_{0.5} were observed at 230.7, 245.4, 254.7, and 358.7, 417.2, 436.6 cm⁻¹, corresponding to the out-of-plane A_g¹, in-plane B_{2g}, and out-of-plane A_g² modes for the “As,” and the A_g¹, B_{2g}, and A_g² modes for “P.” These results align with previous reports^[23]. The X-ray diffraction (XRD) pattern in Fig. 1(c) reveals the crystallographic information of the b-As_{0.5}P_{0.5} flake layer, with diffraction peaks at approximately 17°, 34°, and 51°, corresponding to the (020), (040), and (060)

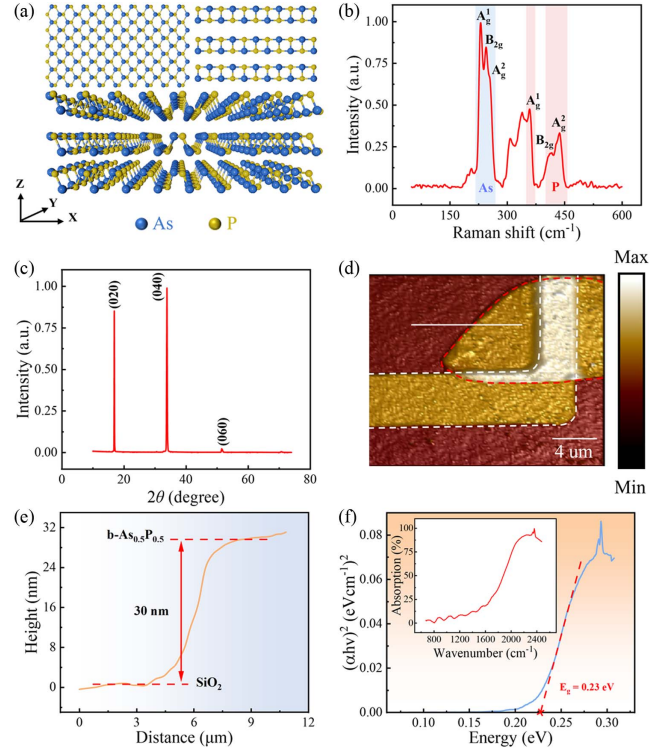


Fig. 1. (a) Crystal structure of the 2D b-As_{0.5}P_{0.5} layers. First row: top view and right view; Second row: side view. (b) Raman spectra of the 2D b-As_{0.5}P_{0.5} layers. (c) XRD pattern of the 2D b-As_{0.5}P_{0.5} layers. (d) Atomic force microscopic image of the PDs. White dashed line: metal electrode; red dashed line: b-As_{0.5}P_{0.5} material. (e) Height profile obtained along with the white line in (d). (f) Tauc plot of the b-As_{0.5}P_{0.5} PDs. The inset shows the FTIR spectra of the PDs.

crystal planes, respectively. These diffraction results are consistent with previous reports^[25], confirming good crystallinity of the material. Figure 1(d) presents an atomic force microscopic image of the surface of b-As_{0.5}P_{0.5}, revealing a layered structure, which suggests the potential formation of stepped growth features during b-As_{0.5}P_{0.5} fabrication. Figure 1(e) presents the height profile obtained along the white line in Fig. 1(d), indicating a b-As_{0.5}P_{0.5} thickness of approximately 30 nm, as b-AsP becomes more difficult to exfoliate with increasing arsenic content. To study the absorption properties and bandgap of b-As_{0.5}P_{0.5}, we obtained its absorption profile using a Fourier transform infrared (FTIR) spectrometer, as depicted in the inset of Fig. 1(f). This absorption profile was then used to generate the Tauc plot, as shown in Fig. 1(f),

$$(\alpha hv)^{1/n} = A(hv - E_g), \quad (1)$$

where α is the absorption coefficient, h is the Planck's constant, ν is the frequency, A is a constant, E_g is the semiconductor bandgap, and n is related to the type of semiconductor^[26,27]. Since b-As_{0.5}P_{0.5} is a direct bandgap semiconductor, $n = 1/2$. Based on this, the estimated bandgap of b-As_{0.5}P_{0.5} is approximately 0.23 eV, consistent with previous reports^[28]. This narrow bandgap enables b-As_{0.5}P_{0.5} to respond to longer-wavelength IR

photons, corresponding to $\sim 5.4 \mu\text{m}$, which extends into the mid-wave infrared band, offering broad potential applications in IR detection.

The synthesized black arsenic-phosphorus was mechanically exfoliated to generate high-quality flake samples. The $\text{b-As}_{0.5}\text{P}_{0.5}$ flakes were subsequently processed using photolithography and deposition to prepare the $\text{b-As}_{0.5}\text{P}_{0.5}$ PDs. Figure 2(a) illustrates the device structure, comprising Cr/Au electrodes (50 nm Au on the top and 5 nm Cr on the bottom), SiO_2 (300 nm), and Si (500 μm) substrates, with a $\text{b-As}_{0.5}\text{P}_{0.5}$ flake positioned between the electrodes. Additionally, due to the presence of phosphorus-phosphorus and arsenic-phosphorus bonds in $\text{b-As}_{0.5}\text{P}_{0.5}$, the performance of the device degrades over time. To mitigate this and improve long-term stability, the device was encapsulated with hBN to protect itself and enhance its electrical performance^[25].

We further examined the variations in photocurrent at different power levels and bias voltages (V_{ds}). Figure 2(b) shows a significant increase in the photocurrent with increasing bias voltage and laser power, indicating that the $\text{b-As}_{0.5}\text{P}_{0.5}$ PDs are highly sensitive to both laser power and bias voltage, exhibiting strong photoresponse characteristics. Moreover, scanning photocurrent mapping was obtained by employing a confocal optical system to reveal the photocurrent generation mechanisms of our PD, as shown in Fig. 2(c). It illustrates the position-dependent photocurrent distribution across the entire channel under a 1 V bias and 1550 nm IR illumination. The photocurrent originates from the entire channel of the PD, confirming PCE as the response mechanism for the $\text{b-As}_{0.5}\text{P}_{0.5}$ PDs. Figure 2(d) shows the energy band diagrams of the $\text{b-As}_{0.5}\text{P}_{0.5}$ and the metal electrode. According to the previously reported results, the conduction band value of the $\text{b-As}_{0.5}\text{P}_{0.5}$ is located at approximately -4.4 eV , and the conduction type is a p-type^[29]. When the

$\text{b-As}_{0.5}\text{P}_{0.5}$ comes into contact with a metal electrode, electron redistribution occurs from the $\text{b-As}_{0.5}\text{P}_{0.5}$ to the metal due to the difference in their work functions. This electron movement aligns the Fermi levels, leading to band bending in the $\text{b-As}_{0.5}\text{P}_{0.5}$ near the interface. Figure 2(e) depicts the generation and propagation of photogenerated carriers under a forward bias voltage. Under IR light illumination, an electron is excited by an incident photon and transitions from the valence band to the conduction band, forming an $e-h$ pair. This pair is rapidly separated at the interface and injected into the electrodes, generating a photocurrent. As shown by the output curve in Fig. S1 in the [Supplementary Material](#), Ohmic contact has been achieved by our device.

For a more objective evaluation of our PD, we numerically calculated the performance of the devices. Figure 3(a) displays the fast time response across different wavelengths (520 to 1650 nm) at a fixed power of 382 μW . Under near-infrared (NIR) illumination, despite a decrease in the switching ratio, the photocurrent shows a significant and rapid transition between the dark state and laser illumination. To analyze the

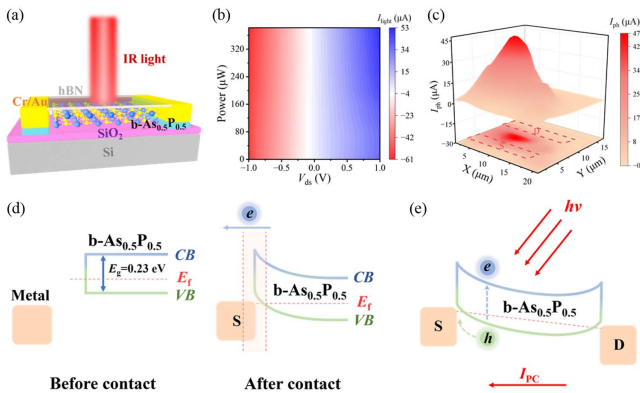


Fig. 2. (a) Schematic diagram of the hBN-encapsulated $\text{b-As}_{0.5}\text{P}_{0.5}$ PDs under IR illumination. (b) The 2D mapping plot of the current under 638 nm laser illumination as a function of the V_{ds} and the incident laser power. (c) The 3D mapping plot of the photocurrent at $V_{\text{ds}} = 1 \text{ V}$ under 1550 nm laser illumination. (d) Energy band diagram of the $\text{b-As}_{0.5}\text{P}_{0.5}$ and the electrode metal (before and after contact). E_f , Fermi level; CB , conduction band; VB , valence band. (e) Energy band diagram of the $\text{b-As}_{0.5}\text{P}_{0.5}$ PD at a bias voltage V_{ds} under illumination. I_{pc} , photoconductive current.

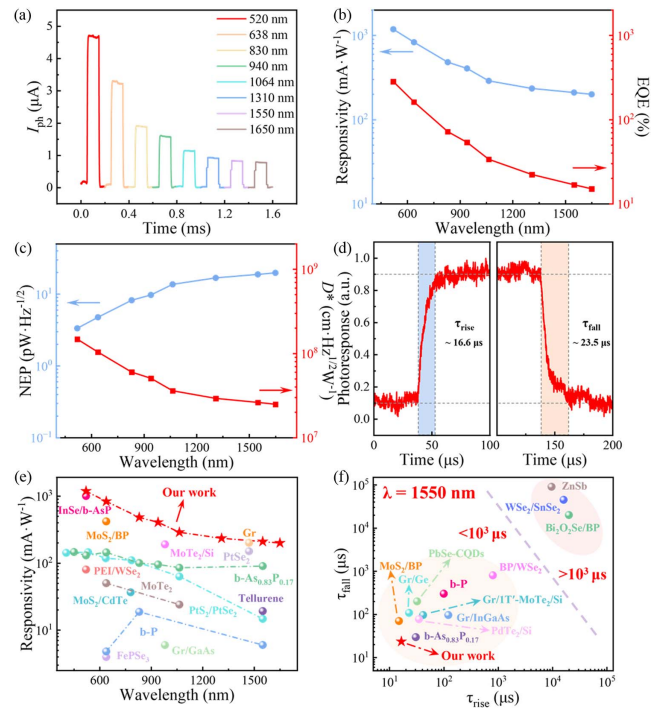


Fig. 3. (a) Temporal photoresponse of the PDs at different wavelengths with fixed incident power at $V_{\text{ds}} = 1 \text{ V}$. (b) Wavelength dependence of the R_i and QE_i at $V_{\text{ds}} = 1 \text{ V}$. (c) Wavelength dependence of the NEP_i and D_i^* at $V_{\text{ds}} = 1 \text{ V}$. (d) Rising and falling times for the PDs under a 1550 nm laser illumination at $V_{\text{ds}} = 1 \text{ V}$. (e) Comparison of the wavelength detection range and the responsivity of our device with other IR PDs [b-P^[33–35], $\text{b-As}_{0.83}\text{P}_{0.17}$ ^[36], Gr^[37], Gr/GaAs^[38], MoTe_2 ^[39], MoTe_2/Si ^[40], MoS_2/BP ^[41], MoS_2/CdTe ^[42], PtSe_2 ^[43], $\text{PtS}_2/\text{PtSe}_2$ ^[44], and Tellurene^[45]]. (f) Comparison of τ_{rise} and τ_{fall} of our device with other IR PDs under a 1550 nm laser illumination [b-P^[46], $\text{b-As}_{0.83}\text{P}_{0.17}$ ^[36], $\text{Bi}_2\text{O}_2\text{Se}/\text{BP}$ ^[47], BP/WSe_2 ^[48], Gr/Ge^[49], Gr/InGaAs^[50], Gr/IT-MoTe₂/Si^[51], MoS_2/BP ^[52], PbSe-CQDs^[53], PdTe_2/Si ^[54], $\text{WSe}_2/\text{SnSe}_2$ ^[55], and ZnSb^[56]].

wavelength-dependent optical response, the responsivity (R) of the detector was calculated as shown in Fig. 3(a),

$$R_i = \frac{I_{ph} S}{P A} = \frac{I_{light} - I_{dark} S}{P A}, \quad (2)$$

where I_{light} is the photocurrent, I_{dark} is the dark current, P is the incident laser power, S is the illuminated area, and A is the device area^[30]. The device area is $24 \mu\text{m}^2$, the illuminated area is $2.29 \times 10^3 \mu\text{m}^2$, and the incident laser power is $382 \mu\text{W}$. Thus, high responsivities (1.182 to $0.199 \text{ A} \cdot \text{W}^{-1}$) were obtained in the visible and near-infrared (Vis-NIR) range. To quantify the light-to-current conversion efficiency, we calculated the external quantum efficiency (EQE), defined as the ratio of charge carriers excited by light to the number of incident photons,

$$\text{EQE}_i = \frac{R_i h c}{\lambda e}, \quad (3)$$

where h is the Planck's constant, c is the speed of light, λ is the wavelength of the incident laser, and e is the electron charge^[31]. The EQE decreases from $\sim 282.1\%$ to $\sim 15.0\%$ as the wavelength increases. At 1550 nm laser illumination, the calculated EQE reaches $\sim 16.7\%$, indicating a satisfactory performance in the NIR range. In our device, noise (I_n) was estimated based on thermal noise (I_{th}) and shot noise (I_{sh}),

$$I_n = \sqrt{\langle i_{th}^2 \rangle + \langle i_{sh}^2 \rangle} = \sqrt{\frac{4k_B T}{R_d} \Delta f + 2qI \Delta f}, \quad (4)$$

where k_B is the Boltzmann constant, T is the temperature, R_d is the resistance, Δf is the operating bandwidth, q is the electron charge, and I is the mean current intensity^[32]. $\langle i_{th}^2 \rangle = 7.79 \times 10^{-25} \text{ A}^2 \cdot \text{Hz}^{-1}$ is obtained at $\Delta f = 1 \text{ Hz}$, at $R_d = 21.3 \text{ k}\Omega$ for the 1 V bias, and at $T = 300 \text{ K}$. At $V_{ds} = 1 \text{ V}$, $I = 45.8 \mu\text{A}$ and $\Delta f = 1 \text{ Hz}$, and $\langle i_{sh}^2 \rangle = 1.47 \times 10^{-23} \text{ A}^2 \cdot \text{Hz}^{-1}$, which is two orders of magnitude higher than the thermal noise level. Therefore, $I_n = 3.93 \times 10^{-12} \text{ A}^2 \cdot \text{Hz}^{-1}$. The noise-equivalent power (NEP) indicates the minimum illumination power that can be detected by the PD, and the specific detectivity (D^*) normalizes the effect of the bandwidth and active area of the PDs with different geometries, enabling better comparison of performance. Thus, the NEP and D^* of our device were calculated^[30] as

$$\text{NEP}_i = \frac{I_n}{R_i}, \quad D_i^* = \frac{\sqrt{A \Delta f}}{\text{NEP}_i}. \quad (5)$$

Figure 3(c) shows that the NEP gradually increases from 3.3 to $19.7 \text{ pW} \cdot \text{Hz}^{-1/2}$ over the wavelength range of 520 to 1650 nm , indicating the ability to detect weak optical signals up to $19.7 \text{ pW} \cdot \text{Hz}^{-1/2}$. Additionally, as the wavelength increases, the specific detectivity decreases from 1.47×10^8 to 2.48×10^7 Jones, reaching up to 1.47×10^8 and 2.61×10^7 Jones for 520 and 1550 nm lasers, respectively. This performance surpasses that of commercial bolometers in certain ranges. Response speed

is another key advantage of PDs. Therefore, the photoresponse time of the device was measured under 1550 nm IR laser illumination. Figure 3(d) shows that the device exhibits a rise time (τ_{rise}) of $\sim 16.6 \mu\text{s}$ and a fall time (τ_{fall}) of $\sim 23.5 \mu\text{s}$ (defined as the time to transition from 10% to 90% and vice versa of the steady photocurrent), demonstrating a rapid response to IR light. This fast response is attributed to the high carrier mobility and short carrier lifetime of the $\text{b-As}_{0.5}\text{P}_{0.5}$, enabling rapid separation of photogenerated carriers and their recombination after the light is turned off, accelerating signal response. As shown in Figs. 3(e) and 3(f), the responsivity and response time of our device were compared with other IR PDs at 1550 nm . Our device demonstrates an excellent short response time and is capable of detecting low-intensity optical signals while maintaining a rapid response. This makes it highly advantageous for high-frequency optical signal detection and NIR wavelength light detection. Compared to other detectors, $\text{b-As}_{0.5}\text{P}_{0.5}$ PDs offer a well-balanced trade-off between responsivity and response time, making them suitable for photodetection applications requiring high sensitivity and fast response. In particular, in the 1550 nm band, our device has approximately 25 times the responsivity and 0.1 times the response time compared to black phosphorus.

Considering the fast response capability of the $\text{b-As}_{0.5}\text{P}_{0.5}$ PDs at 1550 nm , we leveraged this property for NIR optical communication studies. Figure 4(a) presents a schematic diagram of the NIR optical communication system at 1550 nm . After inputting the target information "AsP" into the computer, the characters "A," "s," and "P" were converted into "65," "115," and "80," respectively, based on the American Standard Code for Information Interchange (ASCII). These were then encoded into binaries as "01000001," "01110011," and "01010000." The encoded result was transmitted to a signal generator to modulate the V_{ds} of the PDs between 0 and 1 V , generating a pulsed square wave. Simultaneously, a 1550 nm IR laser continuously

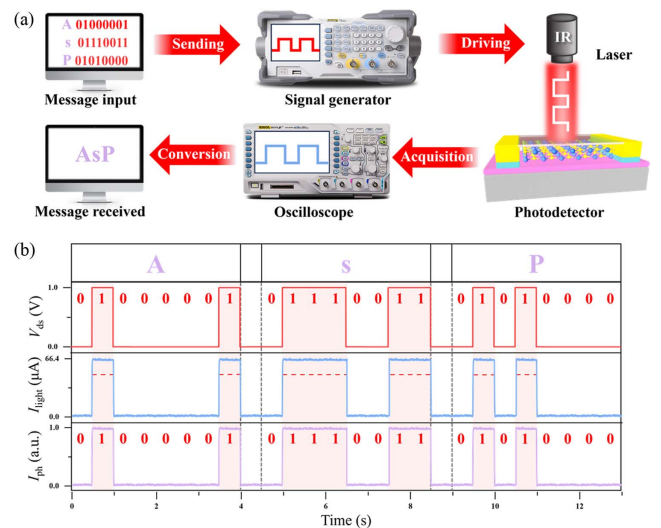


Fig. 4. (a) Schematic diagram of an IR optical communication application. (b) Transmitted ASCII code of "AsP" under a 1550 nm laser illumination. $I_{dark} = 50 \mu\text{A}$.

illuminated the PDs at a constant power of 7.53 mW. The device then converted the modulated pulse bias voltage into a current signal, which was transmitted to a terminal computer via an oscilloscope. Then, the photocurrent was calculated by subtracting the dark current ($I_{\text{dark}} = 50 \mu\text{A}$) from the light current, and the ASCII code for “AsP” was generated by normalizing the photocurrent and was subsequently decoded back to “AsP”^[54,57–59]. Figure 4(b) displays the input, transmitted, and received signals, respectively, and the comparison shows that the received square wave closely matches the original input. This confirms the successful NIR optical communication at 1550 nm, highlighting the great potential of our detector for IR optical communication applications.

Given the excellent IR detection capability of b-As_{0.5}P_{0.5} PDs at 1550 nm, we further explored their application in IR imaging at room temperature ($T = 300 \text{ K}$). Figure 5(a) presents a schematic diagram of the IR imaging measurement system, which uses a single b-As_{0.5}P_{0.5} PD as a sensing pixel without the need for cryogenic cooling. The 1550 nm IR signal was emitted from a laser, passing first through a diaphragm to limit the beam size and range, and then through a hollow “ACSII” mask [Fig. 5(b)] fixed to a 2D translation stage, before illuminating the b-As_{0.5}P_{0.5} PDs. The b-As_{0.5}P_{0.5} PDs converted the IR optical signals into electrical signals, and the corresponding photocurrent magnitudes were recorded by a computer. To achieve single-pixel imaging, the 2D translation stage continuously moved the “ACSII” mask, allowing the IR signal to scan across the entire mask. The corresponding photocurrents at 1550 nm were then mapped using the computer-recorded photocurrents at various positions. As depicted in Figs. 5(c)–5(e), different imaging results were obtained by varying the V_{ds} applied to the b-As_{0.5}P_{0.5} PDs. With higher bias voltages, such as $V_{\text{ds}} = 1 \text{ V}$, the imaging resolution is significantly improved by the b-As_{0.5}P_{0.5} PDs. As the bias voltage increases, the imaging results transition from blurred to clear, with character outlines and details approaching those of the original mask image. These NIR imaging experiments demonstrate the great potential of

b-As_{0.5}P_{0.5} PDs for the development of highly sensitive, room-temperature, and high-resolution NIR image sensor systems.

3. Conclusion

In conclusion, high-quality b-As_{0.5}P_{0.5} was synthesized using the CVT method and by precisely controlling the growth conditions. The fabricated b-As_{0.5}P_{0.5} PDs show a broad photoresponse in the range of 520 to 1650 nm, and the photoresponse is confirmed to be governed by the photoconductive effect. Due to the superior properties and photoconductivity of b-As_{0.5}P_{0.5}, the PDs demonstrate outstanding performance. In the Vis-NIR band, the b-As_{0.5}P_{0.5} PD achieves high responsivities of $1.182 \text{ A} \cdot \text{W}^{-1}$ at 520 nm, $0.829 \text{ A} \cdot \text{W}^{-1}$ at 638 nm, $0.209 \text{ A} \cdot \text{W}^{-1}$ at 1550 nm, and $0.199 \text{ A} \cdot \text{W}^{-1}$ at 1650 nm, with corresponding EQEs of 282.1%, 161.4%, 16.7%, and 15.0%. Additionally, the noise-equivalent power ranged from 3.3 to $19.7 \text{ pW} \cdot \text{Hz}^{-1/2}$, and the specific detectivity ranged from 1.47×10^8 to 2.48×10^7 Jones in the range of 520 to 1650 nm. Notably, the device achieves a response time of $\sim 16.6 \mu\text{s}$ at 1550 nm and real-time optical communication and high-resolution, high-sensitivity single-pixel IR optical imaging at 1550 nm were successfully demonstrated. With its broad-spectrum response, high responsivity, and fast response time, the b-As_{0.5}P_{0.5} PDs show great promise for applications in optical communication and imaging. For infrared detection, infrared filters can be used to block visible light, thus ensuring that the detector mainly responds to the infrared signal and avoids the impact of ambient background light on the measurement results. In future work, a b-As_{0.5}P_{0.5}/MoS₂ heterojunction can be constructed to reduce the dark current and further increase the specific detectivity^[36].

Acknowledgements

This work was supported by the National Natural Science Foundation of China (No. 62105018).

References

1. C. Liu, J. Guo, L. Yu, *et al.*, “Silicon/2D-material photodetectors: from near-infrared to mid-infrared,” *Light Sci. Appl.* **10**, 123 (2021).
2. G. Rao, X. Wang, Y. Wang, *et al.*, “Two-dimensional heterostructure promoted infrared photodetection devices,” *InfoMat* **1**, 272 (2019).
3. H. Wang, Z. Li, D. Li, *et al.*, “Van der Waals integration based on two-dimensional materials for high-performance infrared photodetectors,” *Adv. Funct. Mater.* **31**, 2103106 (2021).
4. U. Adiyani, T. Larsen, J. J. Zárate, *et al.*, “Shape memory polymer resonators as highly sensitive uncooled infrared detectors,” *Nat. Commun.* **10**, 4518 (2019).
5. K. S. Novoselov, A. K. Geim, S. V. Morozov, *et al.*, “Electric field effect in atomically thin carbon films,” *Science* **306**, 666 (2004).
6. K. S. Novoselov, A. K. Geim, S. V. Morozov, *et al.*, “Two-dimensional gas of massless Dirac fermions in graphene,” *Nature* **438**, 197 (2005).
7. Y. Zhang, Y.-W. Tan, H. L. Stormer, *et al.*, “Experimental observation of the quantum Hall effect and Berry’s phase in graphene,” *Nature* **438**, 201 (2005).

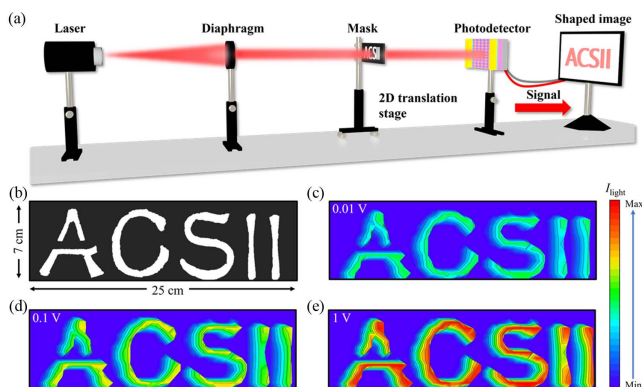


Fig. 5. (a) Experimental setup for single-pixel-based IR imaging with the b-As_{0.5}P_{0.5} PDs under a 1550 nm laser illumination. (b) Optical imaging mask for “ACSII.” (c)–(e) Optical imaging results at different bias voltages ($V_{\text{ds}} = 0.01, 0.1, \text{ and } 1 \text{ V}$).

8. R. Nandee, M. A. Chowdhury, A. Shahid, *et al.*, "Band gap formation of 2D material in graphene: Future prospect and challenges," *Results Eng.* **15**, 100474 (2022).
9. J. Qiao, X. Kong, Z.-X. Hu, *et al.*, "High-mobility transport anisotropy and linear dichroism in few-layer black phosphorus," *Nat. Commun.* **5**, 4475 (2014).
10. T. Vy, R. Soklaski, Y. Liang, *et al.*, "Layer-controlled band gap and anisotropic excitons in few-layer black phosphorus," *Phys. Rev. B* **89**, 235319 (2014).
11. L. Li, Y. Yu, G. J. Ye, *et al.*, "Black phosphorus field-effect transistors," *Nat. Nanotechnol.* **9**, 372 (2014).
12. A. Castellanos-Gomez, L. Vicarelli, E. Prada, *et al.*, "Isolation and characterization of few-layer black phosphorus," *2D Mater.* **1**, 025001 (2014).
13. I. Shirovani, J. Mikami, T. Adachi, *et al.*, "Phase-transitions and superconductivity of black phosphorus and phosphorus arsenic alloys at low-temperatures and high-pressures," *Phys. Rev. B* **50**, 16274 (1994).
14. A. Chauhan, K. Sharma, and S. Choudhary, "Transition metal induced-magnetization and spin-polarisation in black arsenic phosphorus," *Ain Shams Eng. J.* **15**, 102632 (2024).
15. X. Li, J. Luo, H. Yang, *et al.*, "Thermoelectric transport and Rashba spin splitting of black arsenic phosphorus under strain regulation," *Europhys. Lett.* **146**, 56002 (2024).
16. N. D. Zhigadlo, "Exploring 2D materials by high pressure synthesis: hBN, Mg-hBN, b-P, b-AsP, and GeAs," *J. Cryst. Growth* **631**, 127627 (2024).
17. B. Liu, M. Kopf, A. N. Abbas, *et al.*, "Black arsenic-phosphorus: layered anisotropic infrared semiconductors with highly tunable compositions and properties," *Adv. Mater.* **27**, 4423 (2015).
18. J. Liang, Y. Hu, K. Zhang, *et al.*, "2D layered black arsenic-phosphorus materials: Synthesis, properties, and device applications," *Nano Res.* **15**, 3737 (2022).
19. R. Han, S. Feng, D.-M. Sun, *et al.*, "Properties and photodetector applications of two-dimensional black arsenic phosphorus and black phosphorus," *Sci. China Inform. Sci.* **64**, 140402 (2021).
20. Z. Zhu, J. Guan, and D. Tomanek, "Structural transition in layered As(1-x)P(x) compounds: a computational study," *Nano Lett.* **15**, 6042 (2015).
21. Y. Wang, C. Chen, Z. Tang, *et al.*, "Tunable bandgap of black phosphorus by arsenic substitution toward high-performance photodetector," *Sci. China Mater.* **66**, 2364 (2023).
22. F. Liu, X. Zhang, P. Gong, *et al.*, "Potential outstanding physical properties of novel black arsenic phosphorus As(0.25)P(0.75)/As(0.75)P(0.25) phases: a first-principles investigation," *RSC Adv.* **12**, 3745 (2022).
23. B. Karki, M. Rajapakse, G. U. Sumanasekera, *et al.*, "Structural and thermoelectric properties of black arsenic-phosphorus," *ACS Appl. Energy Mater.* **3**, 8543 (2020).
24. F. Zhao, D. Wang, F. Zhang, *et al.*, "Gate-controlled photoresponse improvement in b-AsP/WSe2 heterostructures with type-I band alignment," *Appl. Phys. Lett.* **122**, 151105 (2023).
25. S. Yuan, C. Shen, B. Deng, *et al.*, "Air-stable room-temperature mid-infrared photodetectors based on hBN/black arsenic phosphorus/hBN heterostructures," *Nano Lett.* **18**, 3172 (2018).
26. J. Tauc, R. Grigorovici, and A. Vancu, "Optical properties and electronic structure of amorphous germanium," *Phys. Status Solidi* **15**, 627 (1966).
27. E. A. Davis and N. F. Mott, "Conduction in non-crystalline systems. 5. Conductivity, optical absorption and photoconductivity in amorphous semiconductors," *Philos. Mag.* **22**, 903 (1970).
28. D. Zhuo, C. Jie, Z. H. U. Yi-fan, *et al.*, "Room-temperature terahertz photodetectors based on black arsenic-phosphorus," *Chin. Opt.* **14**, 182 (2021).
29. F. Wu, H. Xia, H. Sun, *et al.*, "AsP/InSe Van der Waals tunneling heterojunctions with ultrahigh reverse rectification ratio and high photosensitivity," *Adv. Funct. Mater.* **29**, 1900314 (2019).
30. Y. Fang, A. Armin, P. Meredith, *et al.*, "Accurate characterization of next-generation thin-film photodetectors," *Nat. Photonics* **13**, 1 (2019).
31. F. Wang, Z. Liu, T. Zhang, *et al.*, "Fully depleted self-aligned heterosandwiched van der Waals photodetectors," *Adv. Mater.* **34**, 2203283 (2022).
32. F. Wang, T. Zhang, R. Xie, *et al.*, "How to characterize figures of merit of two-dimensional photodetectors," *Nat. Commun.* **14**, 2224 (2023).
33. P. K. Venuthurumilli, P. D. Ye, and X. Xu, "Plasmonic resonance enhanced polarization-sensitive photodetection by black phosphorus in near infrared," *ACS Nano* **12**, 4861 (2018).
34. J. Miao, B. Song, Z. Xu, *et al.*, "Single pixel black phosphorus photodetector for near-infrared imaging," *Small* **14**, 1702082 (2018).
35. M. Buscema, D. J. Groenendijk, S. I. Blanter, *et al.*, "Fast and broadband photoresponse of few-layer black phosphorus field-effect transistors," *Nano Lett.* **14**, 3347 (2014).
36. M. Long, A. Gao, P. Wang, *et al.*, "Room temperature high-detectivity mid-infrared photodetectors based on black arsenic phosphorus," *Sci. Adv.* **3**, e1700589 (2017).
37. Y. Zhang, T. Liu, B. Meng, *et al.*, "Broadband high photoresponse from pure monolayer graphene photodetector," *Nat. Commun.* **4**, 1811 (2013).
38. L.-B. Luo, H. Hu, X.-H. Wang, *et al.*, "A graphene/GaAs near-infrared photodetector enabled by interfacial passivation with fast response and high sensitivity," *J. Mater. Chem. C* **3**, 4723 (2015).
39. H. Huang, J. Wang, W. Hu, *et al.*, "Highly sensitive visible to infrared MoTe2 photodetectors enhanced by the photogating effect," *Nanotechnology* **27**, 445201 (2016).
40. Z. Lu, Y. Xu, Y. Yu, *et al.*, "Ultrahigh speed and broadband few-layer MoTe2/Si 2D-3D heterojunction-based photodiodes fabricated by pulsed laser deposition," *Adv. Funct. Mater.* **30**, 1907951 (2020).
41. Y. Deng, Z. Luo, N. J. Conrad, *et al.*, "Black phosphorus-monolayer MoS2 van der Waals heterojunction p-n diode," *ACS Nano* **8**, 8292 (2014).
42. Y. Wang, X. Huang, D. Wu, *et al.*, "A room-temperature near-infrared photodetector based on a MoS2/CdTe p-n heterojunction with a broadband response up to 1700 nm," *J. Mater. Chem. C* **6**, 4861 (2018).
43. X. Yu, P. Yu, D. Wu, *et al.*, "Atomically thin noble metal dichalcogenide: a broadband mid-infrared semiconductor," *Nat. Commun.* **9**, 1545 (2018).
44. J. Yuan, T. Sun, Z. Hu, *et al.*, "Wafer-scale fabrication of two-dimensional PtS2/PtSe2 heterojunctions for efficient and broad band photodetection," *ACS Appl. Mater. Interfaces* **10**, 40614 (2018).
45. C. Shen, Y. Liu, J. Wu, *et al.*, "Tellurine photodetector with high gain and wide bandwidth," *ACS Nano* **14**, 303 (2020).
46. R. Peng, K. Khaliji, N. Youngblood, *et al.*, "midinfrared electro-optic modulation in few-layer black phosphorus," *Nano Lett.* **17**, 6315 (2017).
47. X. Liu, W. Wang, F. Yang, *et al.*, "Bi2O3Se/BP van der Waals heterojunction for high performance broadband photodetector," *Sci. China Inform. Sci.* **64**, 140404 (2021).
48. L. Ye, P. Wang, W. Luo, *et al.*, "Highly polarization sensitive infrared photodetector based on black phosphorus-on-WSe2 photogate vertical heterostructure," *Nano Energy* **37**, 53 (2017).
49. M. G. Kwon, C. Kim, K. E. Chang, *et al.*, "Performance enhancement of graphene/Ge near-infrared photodetector by modulating the doping level of graphene," *APL Photonics* **7**, 026101 (2022).
50. Q. Yang, Q. Wu, W. Luo, *et al.*, "InGaAs/graphene infrared photodetectors with enhanced responsivity," *Mater. Res. Express* **6**, 116208 (2019).
51. D. Wu, C. Guo, L. Zeng, *et al.*, "Phase-controlled van der Waals growth of wafer-scale 2D MoTe2 layers for integrated high-sensitivity broadband infrared photodetection," *Light Sci. Appl.* **12**, 5 (2023).
52. L. Ye, H. Li, Z. Chen, *et al.*, "Near-infrared photodetector based on MoS2/black phosphorus heterojunction," *ACS Photonics* **3**, 692 (2016).
53. P. Chen, Z. Wu, Y. Shi, *et al.*, "High-performance silicon-based PbSe-CQDs infrared photodetector," *J. Mater. Sci. Mater. Electron.* **32**, 9452 (2021).
54. L. Zeng, W. Han, X. Ren, *et al.*, "Uncooled mid-infrared sensing enabled by chip-integrated low-temperature-grown 2D PdTe(2) dirac semimetal," *Nano Lett.* **23**, 8241 (2023).
55. H. Xue, Y. Dai, W. Kim, *et al.*, "High photoresponsivity and broadband photodetection with a band-engineered WSe2/SnSe2 heterostructure," *Nanoscale* **11**, 3240 (2019).
56. R. Chai, Y. Chen, M. Zhong, *et al.*, "Non-layered ZnSb nanoplates for room temperature infrared polarized photodetectors," *J. Mater. Chem. C* **8**, 6388 (2020).
57. C. Wu, G. Zhang, J. Jia, *et al.*, "Highly polarization-deep-ultraviolet-sensitive β -Ga2O3 epitaxial films by disrupting rotational symmetry and encrypted solar-blind optical communication application," *J. Phys. Chem. Lett.* **15**, 3828 (2024).

58. C. Wu, T. Zhao, H. He, *et al.*, “Enhanced performance of gallium-based wide bandgap oxide semiconductor heterojunction photodetector for solar-blind optical communication via oxygen vacancy electrical activity modulation,” *Adv. Opt. Mater.* **12**, 2302294 (2024).
59. H. Xu, Y. Weng, K. Chen, *et al.*, “Ultra-low BER encrypted communication based on self-powered bipolar photoresponse ultraviolet photodetector,” *Adv. Opt. Mater.* **13**, 2402238 (2024).